THE ASTROPHYSICAL JOURNAL, 409:372–386, 1993 May 20

WINDS FROM ACCRETION DISKS: ULTRAVIOLET LINE FORMATION IN CATACLYSMIC VARIABLES

ISAAC SHLOSMAN
Department of Physics and Astronomy, University of Kentucky, Lexington, KY 40506-0055
AND
PETER VITELLO
Physics Department, Lawrence Livermore National Laboratory, Livermore, CA 94550
Received 1992 July 22; accepted 1992 November 16

ABSTRACT

Winds from accretion disks in cataclysmic variable stars are ubiquitous. Observations by *IUE* reveal P Cygni-shaped profiles of high-ionization lines which are attributed to these winds. We have studied the formation of UV emission lines in cataclysmic variables by constructing kinematical models of biconical rotating outflows from disks around white dwarfs. The photoionization in the wind is calculated taking into account the radiation fields of the disk, the boundary layer, and the white dwarf. The three-dimensional radiative transfer is solved in the Sobolev approximation.

Effects on the line shapes of varying basic physical parameters of the wind, such as accretion and mass-loss rates, temperature of the boundary layer, rotation, as well as inclination angle, are shown explicitly. We identify and map the resonant scattering regions in the wind which have strongly biconical character regardless of the asumed velocity and radiation fields. Rotation at the base of the wind introduces a radial shear which decreases the line optical depth and reduces the line core intensity. We find that it is possible to reproduce the observed P Cygni line shapes and make some predictions to be verified in high-resolution observations.

Subject headings: accretion, accretion disks — novae, cataclysmic variables — stars: mass loss

1. INTRODUCTION

Accretion disks on all scales, from active galactic nuclei (hereafter AGNs) to cataclysmic variable stars (CVs) and protostars, appear to be unstable and sustain mass loss from their surface. Several physical processes which can initiate these outflows have been studied: Compton-heated winds (Begelman, McKee, & Shields 1983), hydromagnetic winds (Pudritz & Norman 1985), and line-driven winds (Shlosman, Vitello, & Shaviv 1985). Of these, only the last two are relevant at temperatures low enough to generate UV lines observed from CVs. Both type of winds are expected to build up substantial column densities, sufficient to produce line emission and, possibly, absorption.

Accretion disks around compact objects are predicted to be strong emitters of UV continuum (e.g., Shakura & Sunyaev 1973) and may develop strong magnetic fields (e.g., Galeev, Rosner, & Vaiana 1979). As such, accretion disks should determine the geometry of the outflow, especially at its base. The clustering of strong resonance lines in the UV band as well as large cross sections for interaction between the matter and the radiation at these wavelengths makes it plausible that material above the inner disk will find itself in a super-Eddington regime and will be effectively driven away by a radiation pressure in the UV lines. Such a line-driven wind (LDW) would be accelerated then to terminal velocities of the order of local escape velocity (Vitello & Shlosman 1988, Paper I). Alternatively, at larger distances from the central compact objects or when lower accretion temperatures are encountered, the disks can provide magnetic torques which will act to accelerate the wind to velocities which are few times the local Keplerian motion. Either case will lead to a biconical flow geometry above the disk. We can reverse this statement by saying that a biconical outflow is generally a signature of an accretion disk present in the system.

Line emission is believed to be an efficient diagnostic of physical conditions in different systems, e.g., CVs and AGNs. In this paper we shall limit ourselves to the kinematical models of outflows from accretion disks around white dwarfs (WDs). We are primarily interested in constraints that the UV lines from CVs impose on the velocity field above the disk and on the geometry of the wind. Furthermore, to make our discussion as general as possible, we avoid specifying the driving force behind the wind, although we assume that line radiation transfer in the wind is dominated by resonance scattering of disk continuum photons. When it is useful, we invoke the properties of LDWs. The modeling technique described in this paper has been used to analyze the UV line shapes of CVs observed by the *International Ultraviolet Explorer (IUE)* satellite (Vitello & Shlosman 1993, hereafter Paper II). The emission line profiles for magnetically driven winds in AGNs have been studied separately (Emmering, Blandford, & Shlosman 1992).

In § 2 we discuss the relevant observations of the UV line spectra from CVs. Related aspects in the theory of LDWs from stars and accretion disks are reviewed in § 3. Our kinematic model is explained in § 4, and the radiation transport model in § 5. The results of the modeling and the main conclusions are presented in the last section.

2. OBSERVATIONS OF OUTFLOWS IN CATACLYSMIC VARIABLES

The observational evidence in support of winds in nonmagnetic CVs has been systematically growing during the last decade. Most of it comes from the distinct behavior of the UV lines in luminous CVs: nova-like variables and dwarf novae in outburst. In the intermediate-to-high inclination angle systems the amplitude of UV line modulation is less than that of UV-optical continuum in and out of the eclipse (King et al. 1983;

Córdova & Mason 1985; Kallman 1987; Naylor et al. 1988). Optical frequencies also show signatures of outflows (e.g., Honeycutt, Schlegel, & Kaitchuck 1986; Marsh & Horne 1990). The strongest evidence, however, comes from the P Cygni-shaped profiles of high-ionization UV resonance lines of C IV, N V, and Si IV in low-to-intermediate inclination CV systems with terminal velocities measured up to $\sim$5,000 km s^{-1} (Greenstein & Oke 1982; Guinan & Sion 1982; Córdova & Mason 1982; Klare et al. 1982; and others). Such P Cygni profiles with a blueshifted absorption and a redshifted emission when observed from stars are generally interpreted as of frequency redistribution of stellar continuum photons in an outflow. The closest analogy here is with the outflows from OB stars, which often led to conclusions about similar wind dynamics and dominant spherical geometry. As in these stars, the observed UV line ratios in CVs imply that photoionization and not collisional ionization determines the ionization structure of the wind (e.g., King et al. 1983).

Differences between the line shapes of OB stars and CVs, however, are clearly present. The minimal residual flux in the blueshifted absorption occurs close to the line center in CVs (e.g., Córdova & Howarth 1987), while in OB stars it coincides with the terminal velocity in the wind (e.g., Castor & Lamers 1979). This effect is supported by high-resolution observations: for dwarf-novae (in outburst) and nova-like variables the deepest absorption is at relatively low velocities, e.g., for CD $-42°$ 14462 and CPD $-48°$ at few hundred km s^{-1}, for RW Sex up to 1000 km s^{-1} (Córdova 1986). The strong inclination angle dependence of line profiles in CVs also argues for axisymmetric rather than spherically symmetric intrinsic geometry and, therefore, for a biconical wind associated with a disk and not the central white dwarf. For example, P Cygni line profiles are absent in high-inclination CVs which show more or less symmetric pure emission lines. In addition, P Cygni lines of N V and Si IV differ systematically from lines of C IV by displaying very little or complete absence of emission components. The observations suggest that the volume in which Si IV (and possibly N V) dominates is smaller than that for C IV. This is consistent with the fact that the eclipse depth in the Si IV line is always larger than that of C IV in systems in which the white dwarf is eclipsed by the secondary (King et al. 1983; Córdova & Mason 1985; Drew & Verbunt 1985; Naylor et al. 1988).

Further indirect evidence for the disk origin of these outflows is their apparent absence from magnetic CVs (Kallman 1987), such as AM Her, which are not accreting through the disk. Similarly, signatures of winds in the "intermediate polars," e.g., TV Col (Szkody & Mateo 1984) and DQ Her (Córdova & Mason 1985), may hint for hydromagnetic origin of the wind and its association with the outer disk, at least for this type of objects. The observed wind velocities still can be attained, given that magnetic acceleration may result in higher asymptotic velocities of the wind than radiative acceleration (Emmering et al. 1992). Given the fact that intrinsically luminous CVs are characterized by high accretion rates, hydromagnetic winds can solve the problem of angular momentum removal from the disk.

3. THEORETICAL ASPECTS OF LINE-DRIVEN WINDS FROM STARS AND DISKS

Atmospheres of early-type stars are known to be dynamically unstable. Due to the blanketing effect of the atmospheric UV line opacity, the gas is accelerated to terminal velocities of the order of a few times the escape velocity from a star. The continuum photons are absorbed by UV resonance lines and re-emitted isotropically, hence contributing to the momentum transfer from radiation to the wind. This process can be simply described as a resonant scattering which conserves the number of photons throughout the wind.

The basic theory of stellar LDWs has been worked out in a series of papers by Lucy & Solomon (1970), Castor (1974), Castor, Abbott, & Klein (1975), Cassinelli (1979), Abbott (1980, 1982), Pauldrach, Puls, & Kudritzki (1986) and others (for a review see Abbott 1986). In addition to kinematics and dynamics of the wind, this theory can reproduce correctly the P Cygni profiles of resonance lines, e.g., C III, C IV, Si IV, N V and others, typical for the spectra of OB stars. It is of major importance also that the domain in the parameter space occupied by stars with a blueshifted absorption in UV resonance lines coincides with the domain within which the LDWs have been theoretically found to be self-initiated (Abbott 1979, 1986).

Dynamical modeling of LDWs from accretion disks have been considered first by Shlosman et al. (1985) in analogy with their stellar counterparts. It has been shown that under a broad range of conditions accretion disk atmospheres will become dynamically unstable because the line opacity will effectively put it in the super-Eddington regime. The properties of LDWs from disks have been further investigated by Vitello & Shlosman (1988), who emphasized nonspherical ionizing continuum and driving force as well as a biconical geometry of the outflow. It was found that, in the approximation of vertically streaming radiation (close to the photosphere), disk LDWs are more restrictive than stellar winds and their development is strongly governed by the ionization structure coupled with the thermal balance in the wind. No line fitting was attempted in this study.

Simple kinematical models have been used so far to calculate the UV lines from winds in CVs. All of them share the assumption that the wind emanates radially from the WD. Drew & Verbunt (1985) applied an ionization model within the context of a spherical wind and radiation field, *neglecting* the geometrical effects of the disk. Drew (1987) and Mauche & Raymond (1987) treated radial nonrotating winds in the presence of disk and boundary layer radiation, but assumed *constant* ionization. The above approximations, when used together with a monotonically increasing velocity in the wind, greatly simplify the line radiation transfer; only one resonance scattering surface in the wind exists for the continuum photons under these circumstances and all parameters in the wind depend only on the radial distance from the white dwarf surface. Unfortunately, radial winds require mass-loss rates similar to accretion rates in order to explain the observed UV line profiles, which creates a difficult energetic problem for LDWs. We have found also that purely radial outflows for which the ionization structure is calculated have excessive absorption at large inclination angles (as discussed in § 6).

A rough estimate of mass accretion rate in bright CVs (dwarf-novae in outburst, nova-like variables) can be obtained from the (poorly) known bolometric luminosities of these objects: $\dot{M}_a \sim 10^{-8}(L_{\rm bol}/30\ \ L_\odot)(R_{\rm WD}/7 \times 10^8\ \ {\rm cm})(M_{\rm WD}/0.7M_{\rm WD})^{-1}\ M_\odot\ {\rm yr}^{-1}$, assuming that this luminosity comes from the local cooling in the disk and is not reprocessed emission from the white dwarf. Fitting the UV and optical continua to a blackbody accretion disk spectra gives $\dot{M}_a \sim 10^{-7}$–$10^{-8}\ M_\odot\ {\rm yr}^{-1}$ (Szkody 1985; Córdova & Mason 1982).

Application of model atmospheres can reduce this rate by a factor of 10–100 (Wade 1984).

If the continuum photons escape after just a single scattering, the mass loss-to-accretion rate ratio, $\dot{M}_w/\dot{M}_a$, is limited by the momentum transfer from radiation to the wind, i.e., $\dot{M}_w/\dot{M}_a \lesssim v_\infty/c \sim 1\%$–$2\%$. Here v_∞ is the asymptotic velocity of the LDW and c is the speed of light. In this case, the outflow rates in bright CVs are limited to $\lesssim 10^{-2}\dot{M}_a \sim 10^{-9}$–$10^{-11}$ $M_\odot$ yr^{-1}. Inferring the mass-loss rates from the observed line profiles involves a good amount of modeling. As a result, obtained estimates may be highly misleading because of the wrong geometry (e.g., Drew 1986) or wind dynamics. A more realistic wind, which includes rotation, will introduce so-called multiple resonance scattering surfaces (discussed in § 5). In this case the "single scattering" momentum limit on the mass loss may not apply any more. Strictly speaking the amount of linear momentum transferred to the LDW is then limited only by the energy conservation considerations.

Any torque applied by the disk to the wind acts as a centrifugal acceleration. The strongest coupling between the disk and the wind can probably be provided by the magnetic field generated in the disk. Both rotation and poloidal magnetic fields should affect the wind mostly close to the disk, i.e., within the wind's critical point (or Alfvén point for hydromagnetic winds). In a direct analogy with early-type stars, this will probably lead to increased mass loss from the disk and a more shallow velocity law.

4. KINEMATICAL MODELING

To address the flow above the disk, we assume that it possesses axial symmetry and that the flow originates from an annulus of accretion disk around a white dwarf. Because we are only interested here in studying line profiles in the wind, we sacrifice the dynamics on behalf of kinematics. Using a cylindrical system of coordinates, we take the z-axis aligned with the rotation axis of the disk. The r- and ϕ-coordinates are the radial and azimuthal coordinates on the surface of the disk which is assumed to be planar. The wind streamlines are taken to be three-dimensional spirals which start at the disk surface and continue at a constant angle, θ, to the rotation axis, i.e., the streamlines are helices which lie on conical surfaces with constant opening angles. The streamline opening angle varies with the initial radius of its base,

$$\theta = \theta_{\min} + (\theta_{\max} - \theta_{\min})x^\gamma \,. \tag{1}$$

Here $x \equiv (r_0 - r_{\min})/(r_{\max} - r_{\min})$ and r_0 is the radial coordinate of the base of the streamline in the plane of the disk. The value of $\gamma = 1$ was used generally (which corresponds to a linear variation in θ) and will be assumed unless stated explicitly otherwise. The limiting inclination angles of biconical wind, $\theta_{\min}$ and $\theta_{\max}$, occur at the inner and outer boundaries of the wind, $r_{\min}$ and $r_{\max}$, which are calculated using temperature criterion (see below). This geometry is shown schematically in Figure 1.

The velocity in the wind is given in terms of its cylindrical components, v_r, v_ϕ, v_z. Along each streamline $v_r = v_l \sin\theta$ and $v_z = v_l \cos\theta$, where v_l (which is the velocity in the rz-plane) is assumed to be given by a power law function of $l = [(r - r_0)^2 + z^2]^{1/2}$ (the distance from the disk along the conical streamline surface),

$$v_l = v_0 + (v_\infty - v_0)\left[\frac{(l/R_v)^\alpha}{(l/R_v)^\alpha + 1}\right] . \tag{2}$$

The wind parameters v_0 and v_∞ are the initial and asymptotic wind velocities along the streamline. The quantity R_v is the wind acceleration scale height, and α is the power-law constant. The asymptotic velocity was assumed to scale with the *local* escape velocity, $v_{\rm esc} = (2GM_{\rm WD}/r_0)^{1/2}$, at the base of the streamline. For v_0 we use 6 km s^{-1}. A linear velocity law was also incorporated into the model which uses $v_l = v_\infty$ for $l > R_v$. The linear velocity law gives results similar to the power-law form for $\alpha \simeq 1$. We preferred to use the power-law profile in our modeling, because it gives a continuous variation in the derivative of the velocity, and spreads the observed range of Doppler-shifted frequencies from the region of the wind where $l > R_v$ over a more realistic frequency band. The wind orbital velocity is given initially by Keplerian motion, $v_{\phi,0} = (GM_{\rm WD}/r_0)^{1/2}$. The wind is assumed to conserve its specific angular momentum around the rotation axis, i.e.,

$$v_\phi r = v_{\phi 0} r_0 \,, \tag{3}$$

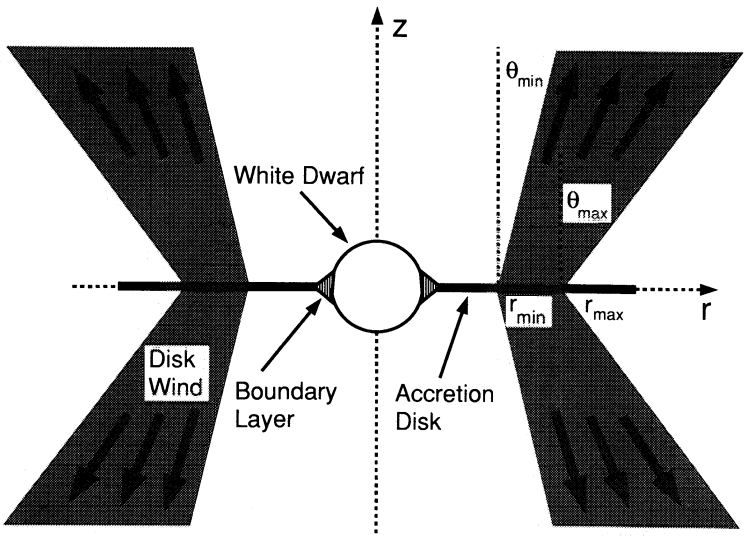

FIG. 1.—Adopted geometry for the disk wind model (not to scale).

as it rises above the disk. The mass loss per unit surface of the disk in the direction of a streamline, $\dot{m}$, at the base radius r_0 was taken to be of the form

$$\dot{m} = \dot{M}_w \frac{r_0^\lambda \cos\theta(r_0)}{\int dA r_0'^\lambda \cos\theta(r_0')}, \quad (4)$$

where the area integral is over the surface of the disk between $r_{\min}$ and $r_{\max}$. Generally we used $\lambda = 0$ which corresponds to a uniform mass loss. The cos θ factor corrects for the fact that the streamlines join the disk at an angle.

The model calculations use a nonlinear grid in r and z, and a linear grid in ϕ with physical quantities such as velocity and density evaluated at cell centers. The z grid is symmetric about the accretion disk, which is assumed to have zero width. The width in z of the first grid cell above (or below) the disk is determined by the height of boundary layer. As this is typically a small region compared to the size of the white dwarf, a single zone is used to span the entire structure. Following the model of Patterson & Raymond (1985), we take the boundary layer zone to have a 45° angle with respect to the disk, with radial extent

$$\left(\frac{H_{BL}}{R_{WD}}\right)^2 \approx 6.29 \times 10^{-4}\left(\frac{M_{WD}}{0.7\ M_\odot}\right)^{-0.85}\left(\frac{\dot{M}_a}{10^{-8}\ M_\odot\ \mathrm{yr}^{-1}}\right)^{0.22} + 4.61 \times 10^{-4}\left(\frac{M_{WD}}{0.7\ M_\odot}\right)^{0.8}\left(\frac{\dot{M}_a}{10^{-8}\ M_\odot\ \mathrm{yr}^{-1}}\right). \quad (5)$$

The outer (r_{BL}^0, z_{BL}^0) grid boundary of the boundary layer, where it joins the disk, is given by $(R_{WD} + H_{BL}, 0)$. The inner (r_{BL}^i, z_{BL}^i) grid boundary, where the boundary layer connects with the white dwarf, is determined by the crossing point of the boundary layer at 45° to the disk with the circle $r^2 + z^2 = R_{WD}^2$. Above the boundary layer, along the z-axis, the grid is set by the following requirement: between $R_{WD} \geq z \geq z_{BL}^i$ the (r, z) grid corresponds to cells of equal area on the white dwarf (i.e., equal spacing in the cosine of the angle with respect to the z-axis). Above the white dwarf the z grid boundaries are logarithmically spaced out to a distance z_b. Beyond $R_{WD} + H_{BL}$ the r grid boundaries are similarly logarithmically spaced out to the distance r_b. Both r_b and z_b are typically 500 R_{WD}. The white dwarf, the boundary layer, and the accretion disk are divided up with linearly spaced cells in ϕ for use in calculating the intensity. The total number of cells in r, z, and ϕ is n_R, n_Z, and n_ϕ, respectively, and values of 100 for each are generally used.

The biconical wind flowing from the annulus $r_{\max}$–$r_{\min}$ on the accretion disk extends over the angular range $\theta_{\max}$–$\theta_{\min}$ with respect to the z-axis. The density in the wind in the first cell above the disk is given by

$$\rho(r_0) = \frac{\dot{m}(r_0)}{v_z(r_0)}. \quad (6)$$

At each point (r, z) in the wind, corresponding to a grid point (i_r, j_z), the local wind parameters were calculated by determining the streamline which passes through this point, i.e., what are the values of r_0 and $\theta(r_0)$. Given (r, z), r_0, and $\theta(r_0)$, the velocity at the point (i_r, j_z) is readily calculated from equations (2)–(3). The local density then follows from the relation

$$\rho(r, z) = \frac{r_0}{r}\frac{dr_0}{dr}\frac{\dot{m}(r_0)}{v_z(r, z)}. \quad (7)$$

In the above equation the term $(r_0/r)(dr_0/dr)$ is due to the increase in area between streamlines as the wind flows from the disk. For streamlines which follow trajectories with a fixed θ cone, we find

$$\frac{dr}{dr_0} = 1 + \frac{l(d\theta/dr_0)}{\cos\theta}. \quad (8)$$

The ionization at each point in the wind was calculated by assuming a constant temperature in the wind ~20,000 K (e.g., King et al. 1983) and local ionization equilibrium. We estimate that, for the C IV ion (from which emission is treated in this paper) and the generic model parameters considered below, ionization equilibrium should be valid until the wind is close to its terminal velocity. Where ionization balance breaks down and the flow time scale becomes shorter than the recombination time scale, the C IV ion population would become constant. However, because far from the white dwarf the decrease of both the photoionization flux and the electron density scale roughly as $1/(r^2 + z^2)$, we find that postulating ionization balance leads to a constant ionization structure in this regime as well.

All ions of H, He, C, N, and O are considered with abundances by number relative to H given by their solar values: $N_{He}/N_H = 0.10$, $N_C/N_H = 3.72 \times 10^{-4}$, $N_N/N_H = 1.5 \times 10^{-4}$ and $N_O/N_H = 6.76 \times 10^{-4}$ (Withbroe 1971). Photoionization by UV photons from the disk, the BL and the WD was calculated taking into account the full three-dimensional radiation field. Collisional ionization and (three-body and dielectronic) recombination (with density-dependent effects) processes are included in the modeling, as well as radiative recombination using a model based on that described in MacGregor & Vitello (1982). The assumption of constant temperature should not lead to large errors in our line profile calculations as the density and radiation field vary much more rapidly than the temperature in the wind.

For comparison purposes, a radial wind model was developed. This model is based on our disk wind model, but has a spherical density profile, streamlines which are radial from the center of the white dwarf, and $v_\phi = 0$ (no rotation). The distance l in the velocity law in equation (2) is now taken to be the radial distance from the white dwarf surface. For the radial wind model we calculate ionization in the wind again using the full radiation field from the white dwarf, boundary layer, and disk. This leads to a highly nonspherical ionization profile.

5. RADIATION TRANSPORT MODEL

To calculate the line radiation transport we use the Sobolev (1957) method modified for a three-dimensional geometry, and described by Rybicki & Hummer (1978, 1983). The radiation propagates in a cylindrically symmetric system with a fully three-dimensional velocity field (v_r, v_z, v_ϕ). We define the monochromatic specific luminosity as $L_\nu \equiv \int dA I_\nu(\hat{n})$. Here $I_\nu(\hat{n})$ is the total intensity along the unit vector $\hat{n}$ which points to the observer, and the area integral is in the plane of the sky normal to $\hat{n}$. In the Sobolev method, scattering of photons emitted at line center frequency ν_0 occurs only at resonant surfaces for which the Doppler-shifted frequency, $\nu_0 + (\nu_0/c)\hat{n} \cdot \boldsymbol{v}$, equals the observed frequency, ν. Rybicki and Hummer have shown that the area integral for L_ν can be replaced with a volume integral,

$$L_\nu = \int d^3\boldsymbol{r} j_\nu(\boldsymbol{r}) \beta_\nu(\boldsymbol{r}, \hat{n}) \quad (9)$$

for which system symmetries can be taken into account. The variables j_v and p_v can be expressed as

$$j_v = k(\mathbf{r})s(\mathbf{r})\delta\left(v - v_0 - \frac{v_0}{c}\,\hat{n}\cdot\boldsymbol{v}\right), \tag{10}$$

and

$$\beta_v = \frac{1 - e^{-\tau(\mathbf{r},\,\hat{n})}}{\tau(\mathbf{r},\,\hat{n})}\, e^{-\sum_{i=1}^{j-1}\tau_i}, \tag{11}$$

where k is the line opacity

$$k = hv_0\, B_{12}\, n_g/4\pi\,, \tag{12}$$

with B_{12} being the Einstein B-coefficient and n_g the number density of ions in the ground state of the resonance line ion. The variable s is the source function. The line optical depth at point $\mathbf{r}$ along the ray $\hat{n}$ is given by $\tau(\mathbf{r}, \hat{n})$. In the Sobolev approximation $\tau(\mathbf{r}, \hat{n})$ is found from the relation

$$\tau(\mathbf{r},\,\hat{n}) = \frac{kc}{4\pi}\,\frac{1}{|Q|}\,, \tag{13}$$

were Q is a quadratic form in the derivatives of the velocity components of the direction vector $\hat{n}$,

$$Q = \sum_{i,j} n_i n_j \frac{\partial v_i}{\partial r_j}\,. \tag{14}$$

The form for $\partial v_i/\partial r_j$ in cylindrical coordinates was taken from Batchelor (1967). The values for the velocity derivatives were calculated at each (r, z) grid point when the velocities were set up. The term in τ_i in equation (11) accounts for the line optical depth at a possible $j - 1$ intervening resonant velocity surfaces between the point $\mathbf{r}$ and the observer. The variable β_v is the local escape probability in the direction $\hat{n}$.

The source function was calculated assuming that only a single resonant velocity surface exists and is given by

$$s(\mathbf{r}) = \frac{(1-\epsilon)\langle\beta_{v_0} I_{v_0}\rangle_{\rm disk} + \epsilon B_{v_0}}{\epsilon + (1-\epsilon)\langle\beta_{v_0}\rangle}\,, \tag{15}$$

where ϵ is the ratio of the collisional de-excitation rate to the radiative de-excitation rate,

$$\langle\beta I_{v_0}\rangle_{\rm disk} = \frac{\int_{\rm disk}\beta_{v_0} I_{v_0}\, d\Omega}{4\pi} \tag{16}$$

is the angular averaged intensity from the disk weighted by the escape probability, and

$$\langle\beta_{v_0}\rangle = \frac{\int \beta_{v_0}\, d\Omega}{4\pi} \tag{17}$$

is the angular averaged escape probability. The quantity B_{v_0} is the blackbody intensity. In calculating $\langle\beta_{v_0}\rangle$ the angular average was done using a 10 point Gaussian integration scheme for both ϕ and θ directions taking into account that $\tau(\mathbf{r}, \hat{n})$ is symmetric in $\hat{n}$. The angular integral for $\langle\beta I_{v_0}\rangle$ was done by summing over the surface cells on the white dwarf, the boundary layer, and the accretion disk. The solid angle for each surface zone (i_{r_0}, j_ϕ) to a first approximation was calculated as $\boldsymbol{A}_{i_{r0}j_\phi}\cdot\hat{n}/d^2$, where $\boldsymbol{A}_{i_{r0}j_\phi}$ is the normal unit vector to the cell times its area, and d is the distance from the point $\mathbf{r}$ to the center of the surface cell. Each surface cell was subdivided until the fractional change in its contribution to $\langle\beta I_{v_0}\rangle_{\rm disk}$ was less than 1%. Such subdivision was necessary for small z as d^2 may be much smaller than the area of the surface cells in the outer regions of the disk. The intensity $I_v(i_{r_0}, j_\phi)$ was calculated assuming blackbody intensities, with the white dwarf and the boundary layer being at fixed assumed temperatures ($T_{\rm WD}$ and $T_{\rm BL}$), and the disk having a radial distribution of surface temperatures given by Shakura & Sunyaev (1973)

$$T_{\rm eff}(r_0) = \left\{\frac{3GM\dot{M}_a}{8\pi\sigma r_0^3}\left[1 - \left(\frac{r_i}{r_0}\right)^{1/2}\right]\right\}^{1/4}, \tag{18}$$

where r_i is the inner radius of the accretion disk, which was taken to be $R_{\rm WD} + H_{\rm BL}$. The wind boundaries, $r_{\rm min}$ and $r_{\rm max}$, are determined using this temperature distribution and correspond to the model parameters $T_{\rm max}$ and $T_{\rm min}$, respectively. We have used the property of a LDW that the line acceleration does not depend on surface gravity, disk thickness, or the effective temperature over the range $10^4 \lesssim T_{\rm eff} \lesssim 5 \times 10^4$ K (Paper I).

Limb darkening is included by weighting the blackbody intensity by the factor $1/2(1 + 3/2\cos\theta)$, where θ is the angle from the normal to the surface of the accretion disk. We assume that the wind density is sufficiently low that radiative decay dominates and set ϵ equal to zero. The single resonant surface approximation used to calculate the source function is known as the disconnected approximation (Marti & Noerdlinger 1977). This approximation tends to underestimate the source function as it ignores possible contributions from other resonant velocity surfaces, but it also neglects the blocking of the disk by intervening portions of multiple velocity surfaces. The scattering region is generally of the same size as the disk emission region. From a study of the topology of the resonant velocity surfaces, we estimate that secondary scattering contributions and blockage would not appreciably modify the source function. Detailed calculations using a Monte Carlo radiative transfer solution for the intensity which self-consistently treats multiple velocity surfaces will be considered in a future paper to study the accuracy of the disconnected approximation for disk winds.

In calculating the line spectrum we evaluate the observed scattered luminosity from the wind and the net unscattered luminosity from the disk separately. The scattered emission was calculated using the volume form for L_v with the source function defined by equation (9). The δ function in j_v allows the volume integral to be reduced to an integral over $r\,dr\,dz$. To be included in the integral, for each point (r, z) there must be at least one value of ϕ, ϕ_R, for which the δ function vanished (i.e., the point (r, z, ϕ_R) lies in a resonant velocity surface). In cylindrical coordinates the condition for a resonant velocity surface at point (r, z, ϕ_R) is that

$$v - v_0 - \frac{v_0}{c}\,[\cos\theta_n v_z(r, z) + \sin\theta_n\cos\phi_R v_r(r, z) - \sin\theta_n\sin\phi_R v_\phi(r, z)] = 0\,, \tag{19}$$

where θ_n is the angle from the axis to the observer who is in the $\phi = 0$ plane. Defining the radial and angular velocities as $v_r \equiv v\sin\theta_v\cos\phi_v$ and $v_\phi \equiv v\sin\theta_v\sin\phi_v$, this relation becomes

$$\cos[\phi_R + \phi_v(r, z)] = \frac{c[(v - v_0)/v_0] - \cos\theta_n v_z(r, z)}{v(r, z)\sin\theta_n\sin\theta_v(r, z)}\,. \tag{20}$$

The variables ϕ_v and θ_v can be found using $\phi_v = \tan^{-1}(v_\phi/v_r)$ and $\theta_v = \sin^{-1}(v_r/v\cos\phi_v)$. For each value of the (r, z) coordi-

nates there are therefore either two, one (the degenerate case), or zero solutions for the ϕ_R-value of the resonant surface. The solutions for ϕ_R are symmetric about the angle $-\phi_v$. When $v_\phi/v_r \gg 1$, $\phi_v \simeq \pi/2$ and the resonant velocity surfaces for a different values of v are elliptical in cross section as is shown in Figure 2*a*. Figure 2 shows contours of $-\boldsymbol{v} \cdot \hat{n}$. The contour values also correspond to the resonant velocity surfaces for $(v_0 - v)/v_0$. Note that positive contours represent motion away from the observer. For a given contour, the surface nearer the observer obscures the farther surface. In the large v_ϕ/v_r limit the angular velocity determines the Doppler frequency and each $(\Delta r, \Delta z)$ ring in the wind makes a double-peaked symmetric contribution to the scattered line intensity with peaks at frequencies $v_0 \pm 2v(r, z)_\phi v_0/c$. When $v_\phi/v_r \ll 1$, $\phi_v \simeq 0$, and the resonant velocity surface is symmetric about the line-of-sight between the center of the disk and the observer and both values of ϕ_R are unobstructed (see Fig. 2*c*). Contributions to the line intensity from each $(\Delta r, \Delta z)$ ring is still symmetric, but now peaks at frequency v_0. The angular velocity decreases along flow lines as the wind expands upwards and outwards from the disk and the radial velocity increases monotonically along the flow lines. The wind thus goes from the $\phi_v \simeq \pi/2$ regime to the $\phi_v \simeq 0$ regime with increasing height above the disk and increasing radial distance outwards. This leads to an opening up of the resonant velocity surface from the rotation-generated elliptical surfaces (see Fig. 2*b*) and an asymmetric contribution to the line intensity. If the velocity surfaces are optically thick then only scattering from the ϕ_R-value for the side closest to the observer is significant. We approximate the possible obscuration of the back of the resonant velocity surface by testing the (x, y) positions for the two values of ϕ_R when $\phi_v > \pi/4$, where $x = r \cos \phi_R$ and $y = r \sin \phi_R$. The luminosity from the point with the more negative value of x is reduced by a factor of $e^{-\tau(r,\hat{n})}$ if both y-values have the same sign. This approximation gives the correct limits for optically thin winds, and for regions where $v_\phi/v_r \gg 1$ and $v_\phi/v_r \ll 1$. Our results were found not to be sensitive to the approximate multiple resonant velocity surface obscuration treatment. In addition to resonant velocity surface blockage, if the ray from the resonant velocity surface projected along $\hat{n}$ passed through the disk or the white dwarf, its contribution was entirely neglected.

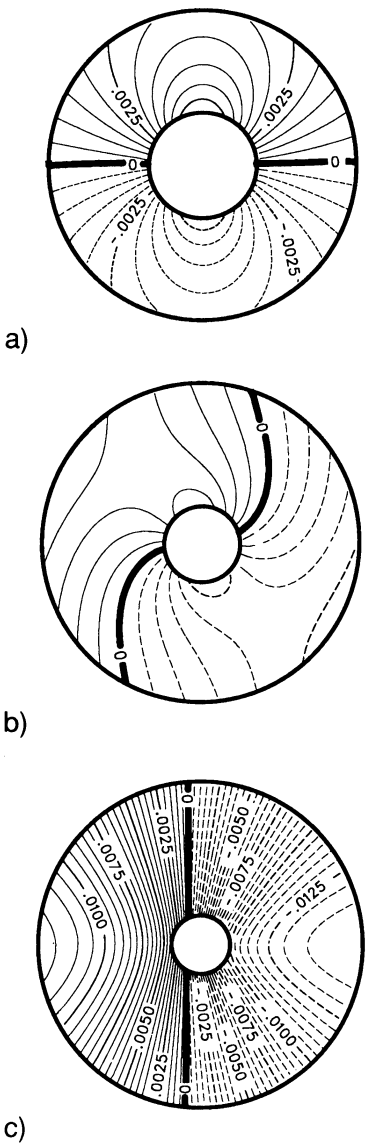

FIG. 2.—Contours at fixed z of $-\hat{n} \cdot \boldsymbol{v}$ showing the resonant velocity surfaces. The inclination $i = 80°$ is used to maximize the observed rotational effects. The contour spacing is 0.0005, with solid contours representing positive values and dashed contours negative values. Figs. 2*a*, 2*b*, and 2*c* correspond to z-values, respectively, of 1 R_{WD}, 13 R_{WD}, and 190 R_{WD}. The figures are scaled to the same size.

For the contribution of the white dwarf, the BL, and the disk to the luminosity at the frequency v, we use the area form for L_v, summing over the upper surface zones. Rays from each zone were followed in the direction $\hat{n}$. The intensity is decreased by a factor of $e^{-\tau(r,n)}$ whenever the ray crosses resonant velocity surfaces. Multiple resonant velocity surfaces were therefore treated in detail for this luminosity component. If the projected ray passed through the white dwarf, its contribution was neglected.

6. DISCUSSION

To demonstrate the line profiles which occur in disk winds we use the generic set of parameters for a CV given in Table 1 and treat the C IV resonance line. These parameters are similar to the large accretion rate model for RW Sex described in Paper II. In Paper II we explore a wider range of parameters which show a greater spatial variation in the C IV ion abundance than is evident in the present study. We assume in our

TABLE 1

GENERIC CATACLYSMIC VARIABLE MODEL

Parameter	Value
M_{WD} ($M_\odot$)	0.8
R_{WD} (cm)	7×10^8
T_{WD} (K)	40,000
T_{BL} (K)	10,000
M_a ($M_\odot$ yr^{-1})	1.0×10^{-8}
M_w ($M_\odot$ yr^{-1})	1.0×10^{-9}
θ_{min}; θ_{max}	20°; 65°
R_d	34 R_{WD}
r_{min}; r_{max}	4 R_{WD}; 12 R_{WD}
T_{min}; T_{max} (K)	20,000; 40,000
R_v	100 R_{WD}
v_∞; α	3 v_{esc}; 1.5

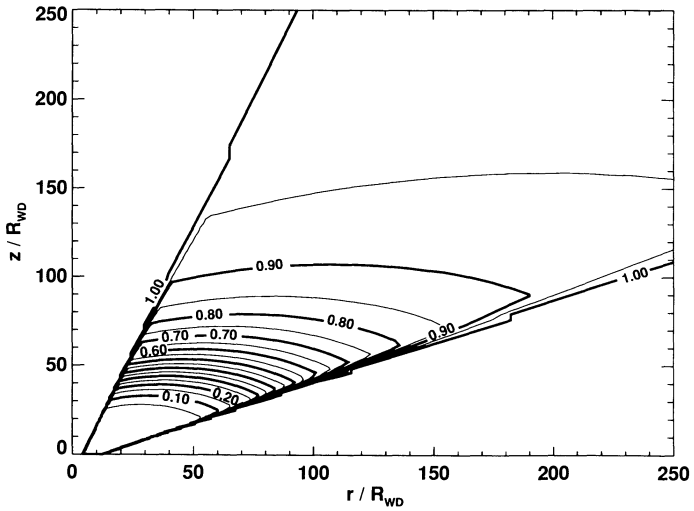

FIG. 3.—Contours of angle-averaged Sobolev escape probability for the ground state of C IV (generic model given in Table 1).

generic models that the BL has little effect on the ionization balance in the wind due to the large optical depth and therefore use a low value of $T_{BL} = 10{,}000$ K unless stated explicitly otherwise. The effects of varying T_{BL} as well as extensive variations in other parameters about the generic model are described below.

Our typical model wind is initially very optically thick to the C IV line, with the local angle-averaged Sobolev escape probability $\langle(1 - e^{-\tau})/\tau\rangle$, much less than unity, as shown in Figure 3. The escape probability increases to $\frac{1}{2}$ at a distance $\simeq 50R_{WD}$ above the accretion disk. This occurs well before terminal velocity is reached. The rapid drop in the escape probability beyond this point is due the decrease in the wind of both the density and the ground state ionization fraction of C IV line, ξ. The model line spectrum is not sensitive to changes in local density or ionization state in regions of the wind which are optically thick. As is shown in Figure 4, ξ is $\ll 1$ very close to the disk, peaks at the value $\simeq 70\%$ at $\simeq 2R_{WD}$ above the accretion disk, and decreases quickly with increasing height. This rapid variation in ξ is due primarily to increasing photoionization as the exposure of the wind to the central source grows. Close to the disk the ionizing flux is strongly dependent on the projected surface area of the central emitting region of the disk and on limb darkening. Far above the disk, we find a near spherical $1/(r^2 + z^2)$ variation in the flux.

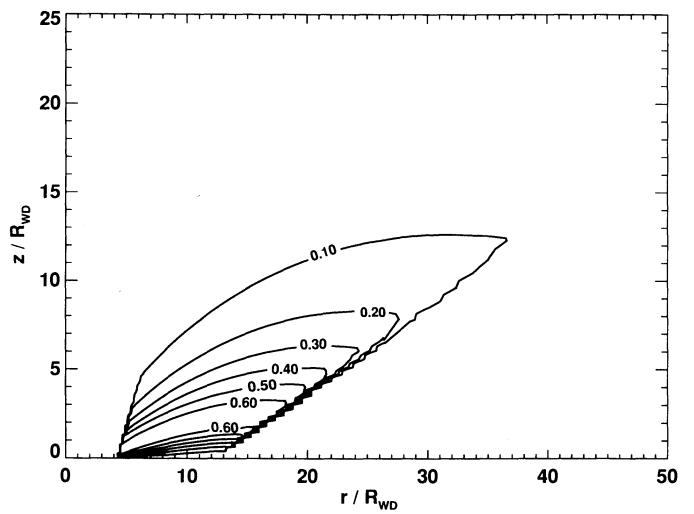

FIG. 4.—Ionization contours for the ground state of C IV of the generic model (Table 1).

In Figure 5 we show the model line profile, scaled to the continuum, as a function of inclination angle i. For our model conditions, the major contribution to the UV flux near 1550 Å comes from the accretion disk. For small i (Fig. 5*a*), the inclination angle is smaller than the inner opening angle of the wind, $\theta_{min} = 20°$. The central dip in the line profile is caused by a combination of absorption and a minimum in the scattered emission near the line center. For $i \lesssim \theta_{min}$, absorption occurs only near the line center where the slowly moving base of the wind obscures a small fraction of the inner disk emission. There is an emission minimum near line center at small i due to geometric effects. Regions of the wind with low velocities relative to the observer occur, for small i, only close to the disk where limb darkening and small projected surface area of the disk, as seen from the WD, deplete the central photon flux. For $i \gtrsim 40°$ the minimum in the scattered emission contribution to the line profile vanishes, but this is hidden due to the effect of absorption. The emission line for large i (Fig. 5*h*) is nearly symmetric in the wings which extend both to the blue and to the red from the line center. For our generic model, the shadowing of the redshifted emission wing by the disk for $i = 80°$ is comparable to the reduction of the blueshifted emission wing by absorption in the wind. For small i, rotational effects in the wind are minimal and absorption is seen only in the blue wing. With increasing i (Figs. 5*b*–5*f*), a deep blueshifted absorption profile becomes evident as the observer views the accretion disk through the disk wind. The sharp rise in the absorption profile to the continuum at small wavelengths is due to finite absorption in regions of the wind near terminal velocity. This outer region of the wind is well resolved spatially by our model. Note that the maximum width of the absorption profile decreases with increasing i. For our disk wind model, the terminal velocity in the wind scales with the local escape velocity at the base of the streamline and, therefore, decreases with increasing radius. The projected maximum velocity towards the observer is maximum when $i \sim \theta_{min}$, and decreases for larger i. The redshifted emission component of the line profile becomes very prominent at large i (Figs. 5*f*–5*h*), while the absorption component abruptly vanishes. The enhancement of the scattered emission profile over the disk continuum is due to the cos i projection effect of the disk and to our use of limb darkening. As for $i < \theta_{min}$, when the disk is viewed from outside of the wind for $i > \theta_{max}$ absorption is greatly diminished except a residual near the line center (Fig. 5*g*). For very large i (Fig. 5*h*), the absorption component of the line has been completely overwhelmed by emission and is not evident. At large inclination angles the wind rotational velocity strongly modifies the projected resonant velocity surfaces. This results in a pronounced asymmetry in the emission line profile near the emission peak (see Fig. 5*h*), with less emission at shorter wavelengths to the line center.

The model line profiles vary as a function of accretion rate and mass-loss rate. The effect of varying $\dot{M}_w$ is straightforward as this changes the wind density, and hence the ionization balance and optical depth. Increasing $\dot{M}_a$ has a direct effect on the ionization balance by increasing the luminosity and photoionization rate. The disk temperature also increases with $\dot{M}_a$. Since the disk boundaries of the wind are fixed by the tem-

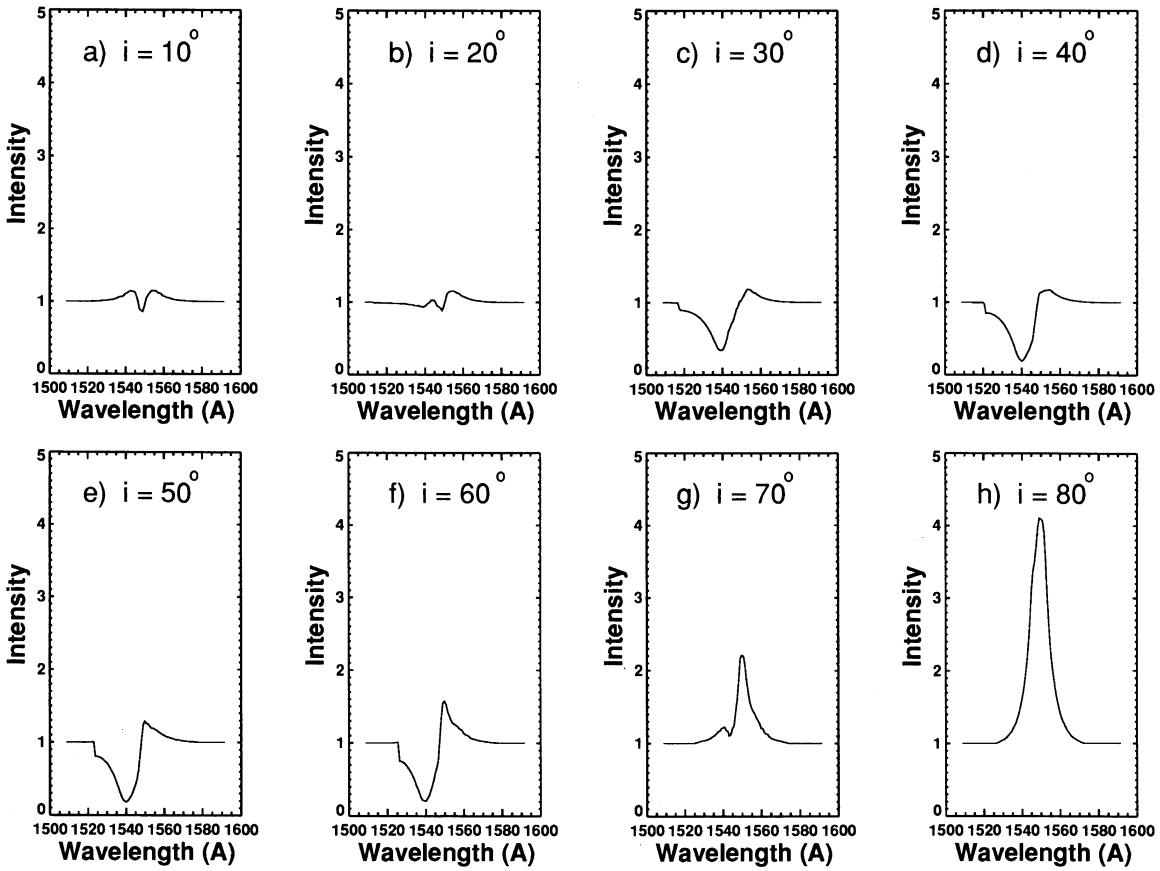

FIG. 5.—Line profiles for the generic model (Table 1) as a function of inclination angle.

perature range, T_{min} to T_{max}, the wind emission region moves outward with increasing accretion rate. This increases the base area for the wind and leads to lower densities and increased ionization. Winds from farther out in the disk also have lower wind velocities, with a narrower resultant line profile. The transition from an optically thick line profile to an optically thin line can therefore occur either by decreasing $\dot{M}_w$ or by increasing $\dot{M}_a$. In Figures 6–10 we show the variation in the line profile as a function of both $\dot{M}_a$ amd $\dot{M}_w$ for several inclination angles. For the largest mass-loss rate shown, $\dot{M}_w = 10^{-8}\ M_\odot\ \mathrm{yr}^{-1}$, the line is saturated with maximum absorption and emission. In Figure 6 ($i = 10°$) we see, as expected, that the symmetric emission profile becomes more prominent with increasing $\dot{M}_w$ or decreasing $\dot{M}_a$. The small blueshifted absorption near line center comes from the base of the wind where the density is greatest and the line optical depth remains high over the range of accretion and mass-loss rates shown. An emission line with a prominent minimum at line center for a low inclination CV would strongly indicate the existence of a disk type wind. The small probability of observing CV systems with small i would make observation of such line profiles infrequent.

With increasing i, strong blueshifted absorption profiles dominate the line spectra. In Figures 7–9 we show the effects of varying $\dot{M}_a$ and $\dot{M}_w$ for $i = 27°.5$–$62°.5$. As the accretion rate is increased or the mass-loss rate is decreased from our generic model, the line profile goes from P Cygni to pure absorption as the emission component disappears. Due to rotation, there is appreciable absorption at longer wavelengths about the line center as well as at shorter wavelengths. Complex absorption line profiles due to the combined v_r, v_z, and rotational v_ϕ components of the Doppler-shifting in the wind can be seen (Figs. 7*d*–7*f*, 9*d*–9*f*). These features would be observable using high-resolution instruments such as the *HST*. For small accretion rates and high mass-loss rates there is, in addition to the absorption profile, a strong redshifted emission component. The width of this component is initially less than that for the absorption profile, and the absorption profile shows maximum absorption near the line center. For larger optical depths (smaller $\dot{M}_a$ or larger $\dot{M}_w$) the emission profile becomes broader than the absorption profile as emission fills in the absorption profile, moving the observed absorption minimum to the maximum blueshifted Doppler wavelength.

For even larger inclination angles the absorption component of the line is submerged by emission. In Figure 10 is shown line profiles for $i = 80$. For $\dot{M}_a = 10^{-7}\ M_\odot\ \mathrm{yr}^{-1}$ (Fig. 10*e*) the optical depth in the wind is sufficiently low that a rotation-generated double-peaked emission profile is evident. For higher optical depths the double peak is not seen because emission from extended flow normal to the disk (where rotation is not significant) fills in between the peaks.

The synthetic line profiles were found to have a fairly weak dependence on the choice of the velocity power-law parameter α and length scale R_v. In Figure 11 we show the variation in the profile at different inclination angles as either α or R_v is changed. The effects of increasing α for fixed R_v or of increasing R_v with fixed α are similar. For $l < R_v$ both lead to increased densities and slower v_r, v_z velocities. This results in more emission and absorption near the line center. Small values of α or of

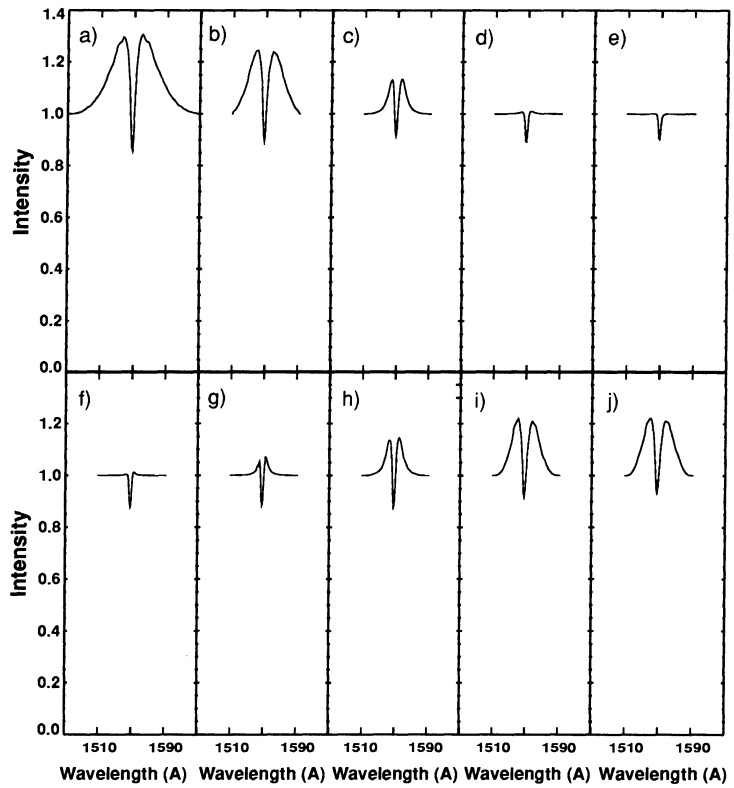

FIG. 6.—Line profiles as a function of $\dot{M}_a$ (*a–e*) and $\dot{M}_w$ (*f–j*) for $i = 10°$. The values for $\dot{M}_a$ (in units of $M_\odot$ yr^{-1}) are 10^{-9}, 3×10^{-9}, 10^{-8}, 3×10^{-8}, and 10^{-7} for Figs. 6*a*–6*e*. The values for $\dot{M}_w$ (in units of $M_\odot$ yr^{-1}) are 10^{-10}, 3×10^{-10}, 10^{-9}, 3×10^{-9}, and 10^{-8} for Figs. 6*f*–6*j*. All other model parameters are given in Table 1.

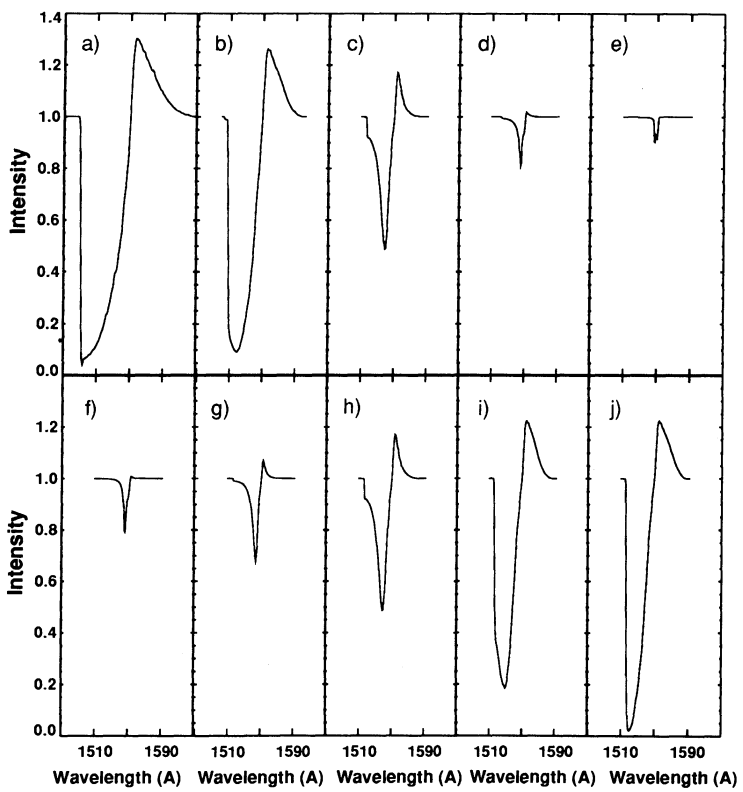

FIG. 7.—Line profiles as a function of $\dot{M}_a$ (*a–e*) and $\dot{M}_w$ (*f–j*) for $i = 27°.5$. The values for $\dot{M}_a$ (in units of $M_\odot$ yr^{-1}) are 10^{-9}, 3×10^{-9}, 10^{-8}, 3×10^{-8}, and 10^{-7} for Figs. 7*a*–7*e*. The values for $\dot{M}_w$ (in units of $M_\odot$ yr^{-1}) are 10^{-10}, 3×10^{-10}, 10^{-9}, 3×10^{-9} and 10^{-8} for Figs. 7*f*–7*j*. All other model parameters are given in Table 1.

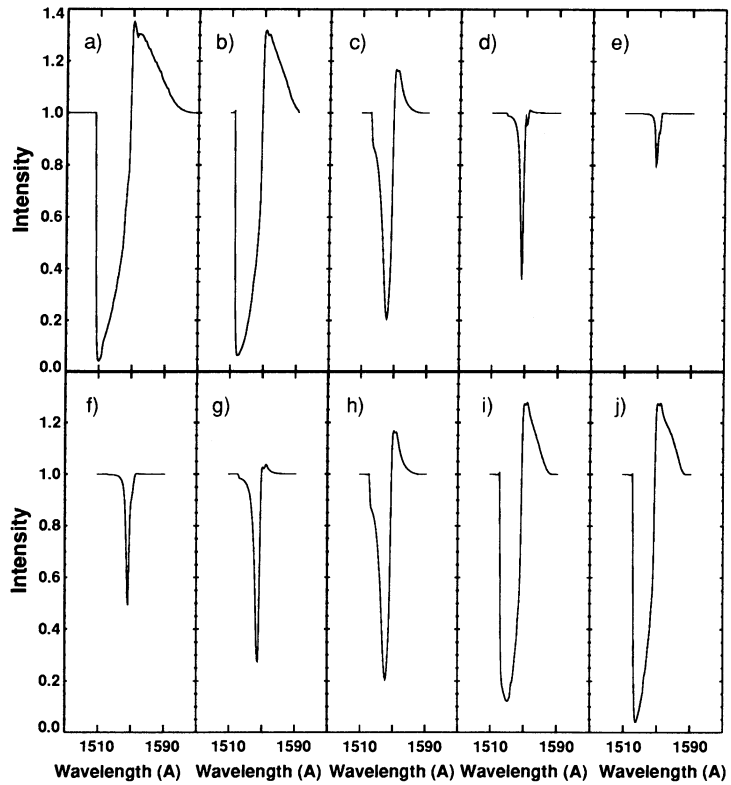

FIG. 8.—Line profiles as a function of $\dot{M}_a$ (*a–e*) and $\dot{M}_w$ (*f–j*) for $i = 45°$. The values for $\dot{M}_a$ (in units of $M_\odot$ yr^{-1}) are 10^{-9}, 3×10^{-9}, 10^{-8}, 3×10^{-8}, and 10^{-7} for Figs. 8*a*–8*e*. The values for $\dot{M}_w$ (in units of $M_\odot$ yr^{-1}) are 10^{-10}, 3×10^{-10}, 10^{-9}, 3×10^{-9}, and 10^{-8} for Figs. 8*f*–8*j*. All other model parameters are given in Table 1.

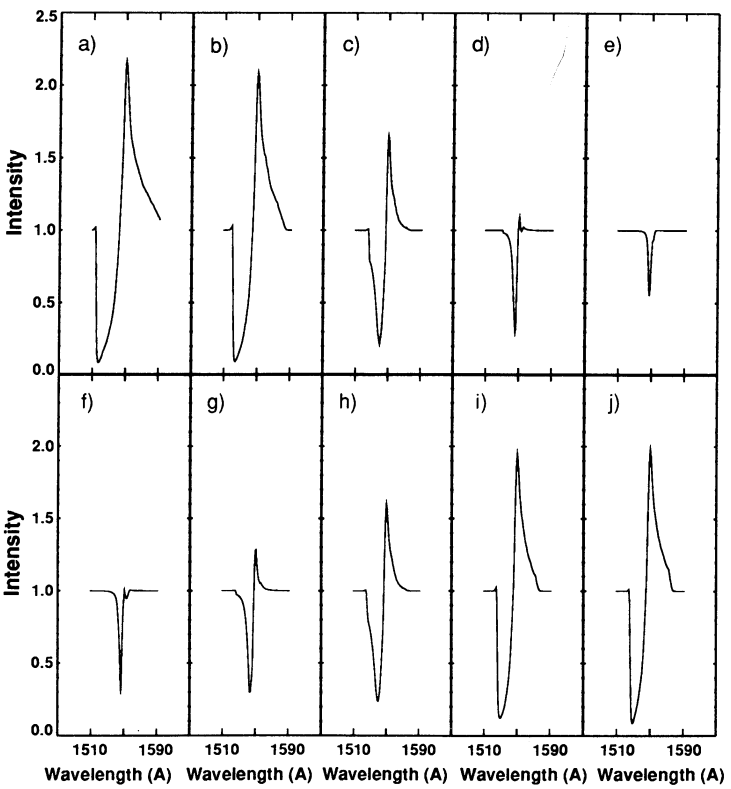

FIG. 9.—Line profiles as a function of $\dot{M}_a$ (*a–e*) and $\dot{M}_w$ (*f–j*) for $i = 62°.5$. The values for $\dot{M}_a$ (in units of $M_\odot$ yr^{-1}) are 10^{-9}, 3×10^{-9}, 10^{-8}, 3×10^{-8}, and 10^{-7} for Figs. 9*a*–9*e*. The values for $\dot{M}_w$ (in units of $M_\odot$ yr^{-1}) are 10^{-10}, 3×10^{-10}, 10^{-9}, 3×10^{-9}, and 10^{-8} for Figs. 9*f*–9*j*. All other model parameters are given in Table 1.

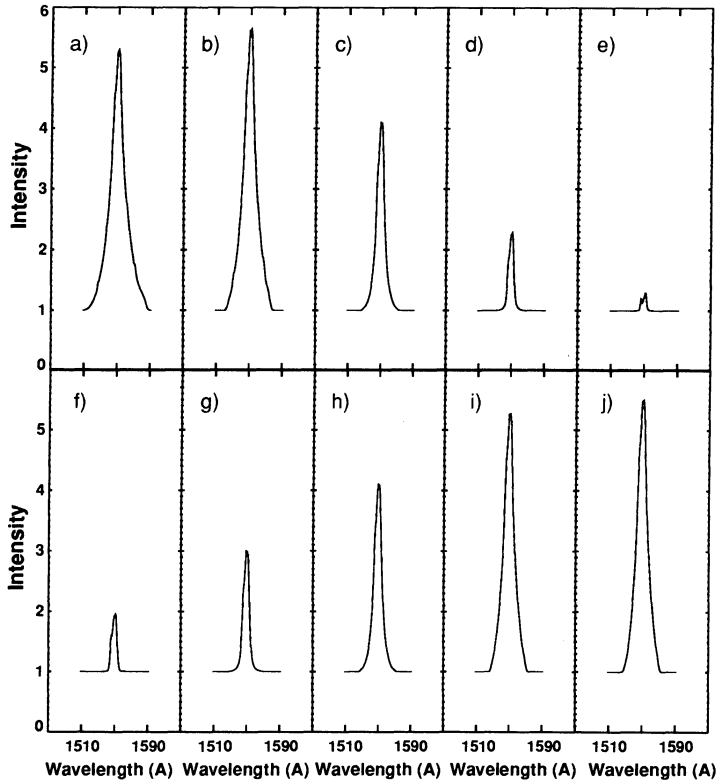

FIG. 10.—Line profiles as a function of $\dot{M}_a$ (*a–e*) and $\dot{M}_w$ (*f–j*) for $i = 80°$. The values for $\dot{M}_a$ (in units of $M_\odot$ yr^{-1}) are 10^{-9}, 3×10^{-9}, 10^{-8}, 3×10^{-8}, and 10^{-7} for Figs. 10*a*–10*e*. The values for $\dot{M}_w$ (in units of $M_\odot$ yr^{-1}) are 10^{-10}, 3×10^{-10}, 10^{-9}, 3×10^{-9}, and 10^{-8} for Figs. 10*f*–10*j*. All other model parameters are given in Table 1.

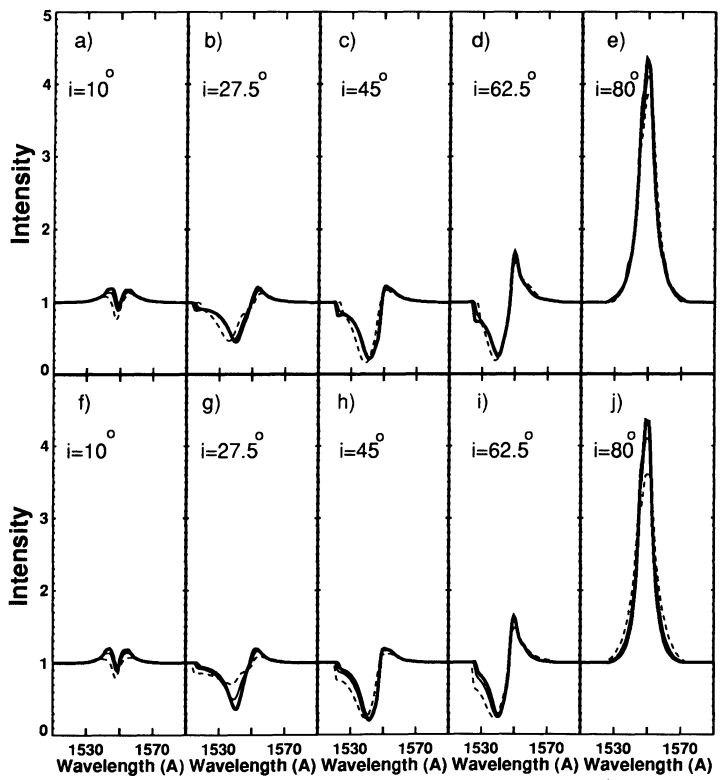

FIG. 11.—Line profiles for different values of *i* showing the effects of varying the wind velocity power-law parameter α (*a–e*) and length scale R_v (*f–j*). In Figs. 11*a*–11*e* the dashed, thin, and thick curves correspond to α values of 1.0, 1.5, and 2.0, respectively, with the generic model value of $R_v = 100 R_{WD}$. For Figs. 11*f*–11*j* the dashed, thin, and thick curves similarly correspond to R_v-values of 50 R_{WD}, 100 R_{WD}, and 150 R_{WD}, with the generic model value of $\alpha = 1.5$.

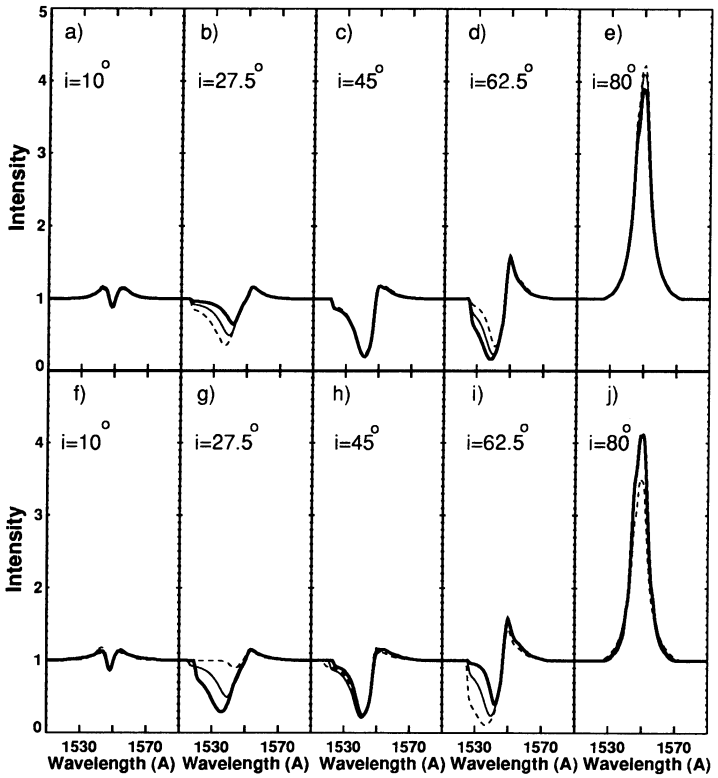

FIG. 12.—Line profiles for different values of i showing the effects of varying the wind mass-loss parameter λ and streamline angle parameter γ. In Figs. 12*a*–12*e* the dashed, thin, and thick curves correspond to λ-values of -1, 0, and 1, respectively, with the generic model value of $\gamma = 1$. For Figs. 12*f*–12*j* the dashed, thin, and thick curves similarly correspond to γ-values of 0.5, 1, and 2, with the generic model value of $\lambda = 0$.

R_v imply a more rapid acceleration for $l < R_v$. This leads to higher densities, and correspondingly larger emission and absorption, at high velocities. The lack of sensitivity to α in our models is most likely due to the broad variation in v_∞ along the flow lines which leads to an effective blending of the velocity structure.

Except for incident angles near $\theta_{\min}$ and $\theta_{\max}$, we find that our model line profiles are not sensitive to the wind parameters λ and γ. In Figure 12 we show the effect of varying these parameters for different inclination angles. Increasing the value of λ leads to the wind mass loss coming preferentially from larger disk radii. This leads to a decrease in the line optical depth for small r and an increase in optical depth at large r. Increasing γ has the opposite effect on the density and optical depth as it causes the streamlines to diverge less for small θ and more for large θ. Figures 12*b* and 12*g* show that for $i \simeq \theta_{\min}$ increasing λ or decreasing γ results in less absorption, while Figures 12*d* and 12*i* show that for $i \simeq \theta_{\max}$ decreasing λ or increasing γ results in less absorption. The emission profile (see Figs. 12*d*, 12*e*, 12*i*, and 12*j*) tends to decrease with increasing λ or decreasing γ. This decreased emission is due to the interior of the wind at small r becoming optically thin. At the same time, the outer portions of the wind (which receive fewer continuum photons due to the effects of limb darkening and the $\cos\theta$ reduction of the disk surface area) become more optically thick, but have fewer photons to scatter.

Variations in the wind terminal velocity were found to strongly affect the blueshifted absorption component of the line profiles, and to a lesser extent the emission width. In Figure 13 is shown how varying v_∞ modifies the line profile at different inclination angles. The dominant effect is the change in position of the blue edge of the P Cygni absorption profile (Figs. 13*b*–13*d*), which shifts to smaller wavelengths as the terminal velocity increases. From Figure 13*e* at $i = 80°$, it is seen that increasing the terminal velocity also broadens the emission component, while also decreasing the line to continuum ratio.

We have studied effects on the line profiles of the various velocity components. The effect of setting $v_\phi = 0$ or $v_l = 0$ is shown in Figure 14. To calculate the profiles for the $v_\phi = 0$ or $v_l = 0$ cases, we first set up the wind using our generic disk wind model for finite values of v_ϕ and v_l (which are used to determine the wind density) and then set the desired velocity equal to zero. This affects the resonant velocity surfaces and the line optical depths. Rotation at the base of the wind introduces a radial shear which decreases the line optical depth and reduces the line core intensity. Without rotational broadening and redshifted absorption due to rotation (i.e., for $v_\phi = 0$), the emission line component of the line profiles is narrower, and is stronger compared to the continuum. This is most evident at large inclination angles. Setting $v_l = 0$ profoundly modifies the line profiles. With only rotation, the wind velocity is less and decreases above the disk. The low velocities lead to a large reduction in the number of continuum photons which can be scattered by the wind and result in weak emission profiles. The low velocities also lead to narrow absorption profiles. With the wind velocity coming only from rotation the model line profiles are symmetric about the line center. Any asymmetry in the curves is due to the discrete wavelength grid used.

Our disk winds are geometrically very different from radial winds. For comparison we have calculated line profiles from a radial wind using the same mass-loss rate, velocity law, and

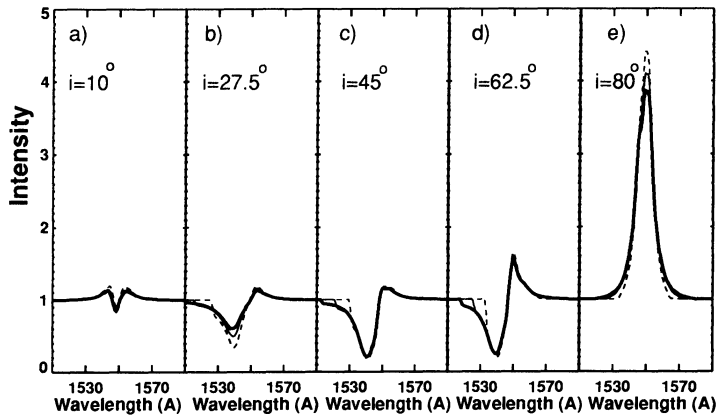

FIG. 13.—Line profiles for different values of i showing the effects of varying the wind terminal velocity parameter v_∞. The dashed, thin, and thick curves correspond to v_∞-values of 2, 3, and 4, respectively.

radiation field for scattering and ionizing as was used for our generic disk wind model. These results are shown in Figure 15. The radial wind profiles show only absorption at small inclination (Figs. 15*a*–15*b*). For the same mass-loss rate, a radial wind with a spherical density distribution has lower density than a biconical disk wind which limits the solid angle of the flow. The lower density for the radial wind results in over-ionization of the C IV ground state at large distances from the disk, and a corresponding reduction of the optical depth, and emission and absorption in the far blue and red wings of the line profile. This is most evident at intermediate inclination angles (Figs. 15*b*–15*d*). To achieve comparable absorption at intermediate inclination angles, radial winds require higher mass-loss rates than disk winds. For large inclination angles (Fig. 15*e*) there continues to be absorption in the radial wind. This is not the case for the disk wind where absorption is reduced for $i > \theta_{\max}$. In Paper II we attempted to fit *IUE* line profiles for the large inclination angle eclipsing binary system RW Tri using our radial wind model. RW Tri shows only an emission profile with no absorption. No acceptable fits were found using the radial model, although we found that excellent agreement could be reached using our disk wind model. The radial wind absorption feature was removed by decreasing the mass-loss rate. This however led to such low densities that the wind became very optically thin at low velocities, and produced a much narrower emission line. The resulting emission line was too narrow compared with the RW Tri spectra.

The temperature of the BL is still very much a matter of controversy. It is expected that if the white dwarf is not rotating close to breakup, then nearly half of the total gravitational potential generated by the accreting matter should be released as radiation in the boundary layer (Lynden-Bell & Pringle 1974). Pringle (1977) and Pringle & Savonije (1979) predicted that for accretion rates typical of nova-like variables and dwarf novae in outburst the value of $T_{\rm BL}$ should be in the range 200,000–500,000 K. Such high values for the boundary layer temperature play havoc with synthetic line modeling by highly over-ionizing the wind, unless the mass-loss rate is unreasonably high (see, e.g., Mauche & Raymond 1987). For our generic model, values of the boundary layer temperatures $\lesssim$80,000 K did not significantly alter the predicted spectra. This is evident from Figure 16 which shows profiles for several values of $T_{\rm BL}$. Emission from the white dwarf similarly had little affect on the line profiles in our simulations. High BL temperatures require increased mass-loss rate to prevent the wind from becoming over-ionized and too optically thin. Hoare & Drew (1991) conclude that typical BL temperatures should range between 50,000–100,000 K, which would lead to only small modifications to the synthetic spectra presented in this paper. Observations of soft X-ray fluxes and ionization state of CV winds

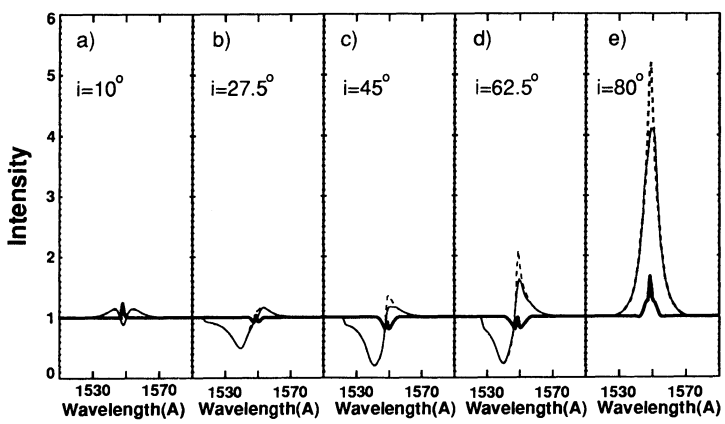

FIG. 14.—Line profiles for different values of i showing the effects of disk winds with v_ϕ or v_l set to zero. The dashed, thin, and thick curves correspond to $v_\phi = 0$, our generic model, and $v_l = 0$.

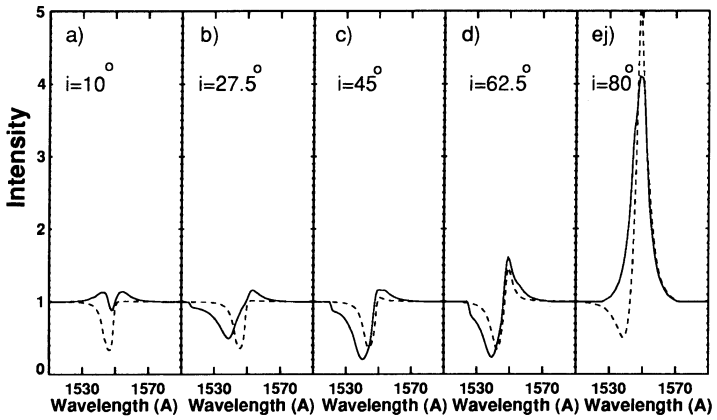

FIG. 15.—Line profiles for different values of i showing the difference between our disk wind and radial outflow. The dashed and solid curves correspond to a radial wind and our generic disk wind model.

point to a lower T_{BL} than the one predicted theoretically as well. Other explanations of the low soft X-ray value, however, such as interstellar and/or photoelectric absorption are also viable (e.g., Raymond & Mauche 1991).

We have found (see Paper II) that our disk wind model, with its free parameters describing the wind geometry, cannot produce a unique fit to the observed profiles on the basis of a kinematical model alone. A true dynamical model for a two-dimensional outflow from a disk should remove this limitation.

7. CONCLUSIONS

We have studied the formation of UV emission lines from accretion disk winds in CVs. A series of kinematical models have been constructed for three-dimensional rotating winds. The continuum photons from the disk, boundary layer, and the white dwarf have been assumed to resonance scatter off the flow resulting in the formation of P Cygni line profiles at some inclination angles and pure emission or absorption at others. The three-dimensional line radiative transfer was performed in the Sobolev approximation. The ionization balance in the wind was found in a manner without assuming a priori LTE.

The main difficulty in using the Sobolev approximation for general geometries is the introduction of multiple velocity scattering surfaces. Although biconical outflows possess an axial symmetry, the presence of a non-negligible rotation (especially at the base of the wind) removes it. We have identified and mapped the resonant scattering regions in the wind which have distinctly biconical character regardless of the assumed velocity law in the flow and geometry of the radiation field.

We have performed a parameter search in order to determine the sensitivity of the model to its basic parameters. We find that rotation affects the line shape at large inclination angles resulting in pronounced asymmetry. The mass accretion and loss rates in CVs also have profound effect on the line shape at every inclination angle. At very low angles, the line is characterized by a narrow dip in the line core which may serve as an indicator of the disk type wind, although its detection probability is slim. At larger inclination angles, a P Cygni profile should be observed, typically dominated by a broad blueshifted absorption. Rotation contributes to a certain amount of redshifted absorption which modifies the line profile and may be detected in principle with high-resolution instruments. At large inclinations, our model lines appear just in emission, with an asymmetric or possibly double peak, depending on the accretion and outflow rates.

The calculated line profiles have quite a weak dependence on the velocity power-law index and the wind length scale, but the width of the blueshifted absorption component and, to a lesser degree that of the emission, are strongly modified by the wind terminal velocity. These, as well as other parameters affect the wind mostly through the ionization balance, directly or indirectly.

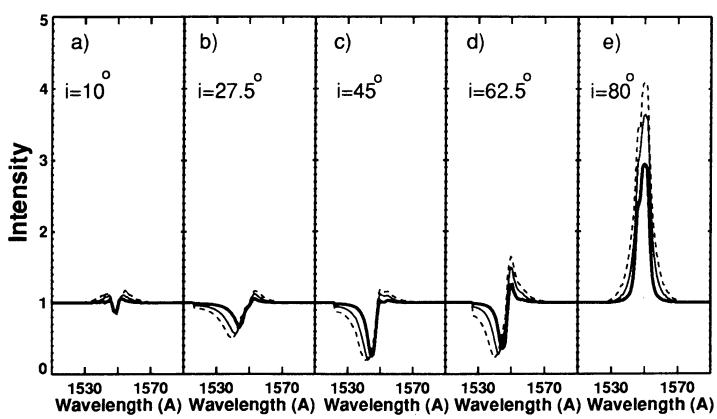

FIG. 16.—Line profiles for different values of i showing the effects of varying the boundary layer temperature. The dashed, thin, and thick curves correspond to T_{BL} values of 75,000 K, 100,000 K, and 125,000 K, respectively.

We find that the disk winds differ substantially from the radial nonrotating winds. For the same outflow rates, the radial winds are overionized and have lower optical depth which reduces the amount of emission and absorption. At large inclination angles radial winds have too much absorption contrary to observations of such systems.

We are grateful to Chris Mauche for many stimulating discussions of observational results. We thank Andrew Hazi, V Division Head at LLNL, for his support. We thank the RDAF staff in Boulder (which is supported by NASA contract NAG5-28731) for their technical assistance. This work was performed under the auspices of the US Department of Energy by LLNL user contract number W-7405-ENG-48 and supported in part by NASA grant NAG5-1387.

REFERENCES

Abbott, D. C. 1979, in IAU Symp. 83, Mass Loss and Evolution of O-Type Stars, ed. P. S. Conti & C. W. de Loore (Dordrecht: Reidel), 237
———. 1980, ApJ, 242, 1183
———. 1982, ApJ, 259, 282
———. 1985, in Proc. Trieste Workshop on Relations between Chromospheric-Coronal Heating and Mass Loss in Stars, ed. R. Stalio & J. B. Zirker (Sunspot, NM: Sacramento Peak Observatory), 265
Batchelor, G. K. 1967, An Introduction to Fluid Mechanics (Cambridge: Cambridge Univ. Press)
Begelman, M. C., McKee, C. F., & Shields, G. A. 1983, ApJ, 271, 70
Cassinelli, J. P. 1979, ARA&A, 17, 275
Castor, J. I. 1974, MNRAS, 169, 279
Castor, J. I., Abbott, D. C., & Klein, R. I. 1975, ApJ, 195, 157
Castor, J. I., & Lamers, H. J. G. L. M. 1979, ApJS, 39, 481
Córdova, F. A. 1986, in The Physics of Accretion onto Compact Objects, ed. K. O. Mason et al. (Berlin: Springer), 339
Córdova, F. A., & Howarth, I. D. 1987, in Scientific Accomplishments of the *IUE*, ed. Y. Kondo (Dordrecht: Reidel), 467
Córdova, F. A., & Mason, K. O. 1982, ApJ, 260, 716
———. 1985, ApJ, 290, 671
Drew, J. 1986, MNRAS, 218, 41P
———. 1987, MNRAS, 224, 595
Drew, J., & Verbunt, F. 1985, MNRAS, 213, 191
Emmering, R. T., Blandford, R. D., & Shlosman, I. 1992, ApJ, 385, 460
Galeev, A. A., Rosner, R., & Vaiana, G. S. 1979, ApJ, 229, 318
Greenstein, J. L., & Oke, J. B. 1982, ApJ, 258, 209
Guinan, E. F., & Sion, E. M. 1982, ApJ, 258, 217
Hoare, M. G., & Drew, J. E. 1991, MNRAS, 249, 452
Honeycutt, R. K., Schlegel, E. M., & Kaitchuck, R. H. 1986, ApJ, 302, 388
Kallman, T. 1987, in Proc. IAU/COSPAR Conf. on The Physics of Accretion onto Compact Objects, ed. K. O. White, M. G. Watson, & N. E. White (Dordrecht: Reidel), 269
King, A. R., Frank, J., Jameson, R. F., & Sherrington, M. R. 1983, MNRAS, 203, 677
Klare, G., Krautter, J., Wolf, B., Stahl, O., Vogt, N., Wargau, W., & Rahe, J. 1982, A&A, 113, 76
Lucy, L. B., & Solomon, P. 1970, MNRAS, 159, 879
Lynden-Bell, D., & Pringle, J. E. 1974, MNRAS, 168, 603
MacGregor, K., & Vitello, P. 1982, ApJ, 259, 267
Marsh, T. R., & Horne, K. 1990, ApJ, 349, 593
Marti, F., & Noerdlinger, P. D. 1977, ApJ, 215, 247
Mauche, C. W., & Raymond, J. C. 1987, ApJ, 323, 690
Naylor, T., et al. 1988, MNRAS, 231, 237
Patterson, J., & Raymond, J. C. 1985, ApJ, 292, 550
Pauldrach, A., Puls, J., & Kidritzki, R. P. 1986, A&A, 164, 86
Pringle, J. E. 1977, MNRAS, 178, 195
Pringle, J. E., & Savonije, G. J. 1979, MNRAS, 187, 777
Pudritz, R. E., & Norman, C. A. 1985, Canadian J. Phys., 64, 501
Raymond, J. C., & Mauche, C. W. 1991, in Extreme UV Astronomy, ed. R. F. Malina & S. Bowyer (NY: Pergamon), 163
Rybicki, G. B., & Hummer, D. G. 1978, ApJ, 219, 654
———. 1983, ApJ, 274, 380
Shakura, N. I., & Sunyaev, R. A. 1973, A&A, 24, 337
Shlosman, I., Vitello, P. A. J., & Shaviv, G. 1985, ApJ, 294, 96
Sobolev, V. V. 1957, Soviet Astron.–AJ, 1, 678
Szkody, P. 1985, in Cataclysmic Variables & Low-Mass X-Ray Binaries, ed. D. Q. Lamb & J. Patterson (Dordrecht: Reidel), 385
Szkody, P., & Mateo, M. 1984, ApJ, 280, 729
Vitello, P. A. J., & Shlosman, I. 1988, ApJ, 327, 680 (Paper I)
———. 1993, ApJ, in press (Paper II)
Wade, R. A. 1984, MNRAS, 208, 381
Withbroe, G. L. 1971, in The Menzel Symposium of Solar Physics, Atomic Spectra, and Gaseous Nebulae, ed. K. B. Gebbie (NBS Spec. Pub. 353), 127